THE CHIP-SCALE ATOMIC CLOCK – RECENT DEVELOPMENT PROGRESS

R. Lutwak*, D. Emmons, T. English, W. Riley
Symmetricom - Technology Realization Center†

A. Duwel, M. Varghese
Charles Stark Draper Laboratory

D. K. Serkland and G. M. Peake
Sandia National Laboratories††

Abstract

We have undertaken the development of a chip-scale atomic clock (CSAC) whose design goals include short-term stability, $\sigma_y(\tau = 1$ hour), of 1×10^{-11} with a total power consumption of 30 mW and an overall device volume of 1 cm^3. The stringent power requirement dominates the physics package architecture, dictating a small (< 5 mm^3) gaseous atomic ensemble interrogated by a low-power semiconductor laser. At PTTI 2002, we reported on initial experimental investigations leading to the decision to employ the coherent population trapping (CPT) interrogation technique. This paper describes our further progress on the CSAC effort, including the development of custom vertical cavity surface emitting laser (VCSEL) sources and techniques for microfabricating miniature cesium vapor cells comprised of anodically bonded silicon and glass. Measurements of the signal contrast and linewidth of both the cesium D1 and D2 resonance transitions are compared, and frequency stability measurements of the CSAC testbed are presented.

INTRODUCTION

We are developing a chip-scale atomic clock (CSAC) with the goal of producing a 1 cm^3 device that can provide a stability of 1×10^{-11} over 1 hour while consuming only 30 mW. While the stability goals are modest, equivalent to $\sigma_y(\tau = 1) = 6\times10^{-10}$, the power and size goals are quite ambitious, each more

* E-mail: *RLutwak@Symmetricom.com*
† 34 Tozer Rd., Beverly, MA 01915, USA
†† Sandia is a multiprogram laboratory operated by Sandia Corporation, a Lockheed Martin Company, for the United States Department of Energy's National Nuclear Security Administration under contract DE-AC04-94AL85000.

than two orders of magnitude smaller than existing technology. Our initial work, reported at this conference last year **[1]**, focused on the general architecture of the physics package, a small cesium gas cell interrogated using the method of coherent population trapping (CPT). In this paper, we report on our continued progress, including comparative spectroscopy of the cesium D1 and D2 CPT resonances and experimental investigations of small silicon-glass resonance cells.

SHORT-TERM STABILITY FIGURE-OF-MERIT

Generally speaking, the short-term stability of any atomic frequency standard is proportional to the resonance linewidth and inversely proportional to the signal-to-noise ratio of the detected signal, i.e.

$$\sigma_y(\tau = 1\text{sec}) \propto \frac{\gamma}{(S/N)_{1\,\text{Hz}}},$$

where γ is the resonance linewidth (FWHM) and $(S/N)_{1\ \text{Hz}}$ is the signal-to-noise ratio, measured in a 1 Hz bandwidth at the modulation frequency, F_{MOD}, typically on the order of $\gamma/2$.

In the following sections, we discuss the phenomena that determine these quantities in the CSAC and the trade-offs that must be made in order to meet the CSAC stability requirements within its power budget. Our goal is to establish a figure-of-merit, ξ, which predicts frequency stability based on spectroscopic measurements of linewidth and signal contrast.

There are many contributions to the overall noise figure of the CSAC, including statistical shot noise of the detected signal, phase noise of the local oscillator, pre-amplifier current and voltage noise, and laser frequency noise. The performance of traditional lamp-pumped vapor cell atomic frequency standards is predominantly limited by statistical shot noise of the detected photocurrent, which is proportional to the square-root of the DC level of detected signal, i.e. $N \propto (\text{DC level})^{1/2}$. In the laser-pumped CSAC, we have the additional noise contribution due to laser frequency (or phase) noise, which is converted to amplitude noise by non-linear resonant scattering from the atomic sample.

The mechanism of FM-AM conversion due to resonant scattering is illustrated schematically in Figure 1. In normal operation, the laser frequency is locked to the peak of the atomic resonance line, where the signal is maximized and the sensitivity to frequency excursions is minimized. However, for small excursions of the laser frequency, which arise due to noise on its bias current, temperature fluctuations, and statistical properties of the vertical cavity surface emitting laser (VCSEL) itself, the amplitude fluctuations on the detected signal increase quadratically with detuning from the peak. Moreover, because the atomic response is nonlinear, the vapor cell effectively mixes noise components at all frequencies, limited only by the intrinsic 5 MHz bandwidth of the atomic response, into the detection band at F_{MOD}. The relative magnitude of this noise process is determined by the inhomogeneous linewidth of the atomic resonance and the frequency noise properties (linewidth) of the VCSEL, and is linearly proportional to the light intensity, i.e. $N \propto$ (DC level).

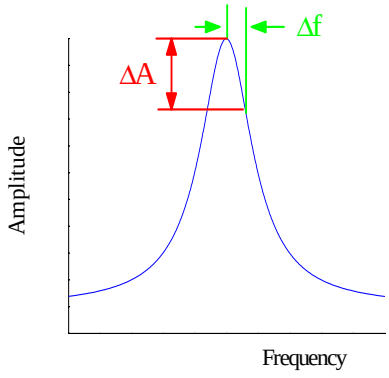

Figure 1. Laser FM→AM noise conversion.

The two principal noise mechanisms, shot noise and laser frequency noise, can thus be differentiated by their power-law dependence on the laser intensity. In order to determine their relative impact in the CSAC device, we've made measurements of noise as a function of DC level in our testbed apparatus.

Figure 2 shows the RMS noise, measured in a 1 Hz bandwidth at 500 Hz, as a function of laser power, over two orders of magnitude spanning the designed operating region of the CSAC. Also shown is a fit to a power law model of (S/N) which indicates $N \propto (\text{DC level})^{0.998}$. We conclude that, for typical CSAC components and operating conditions, the principal noise mechanism in the CSAC is laser frequency noise and, for practical design purposes, $N \propto$ (DC level).

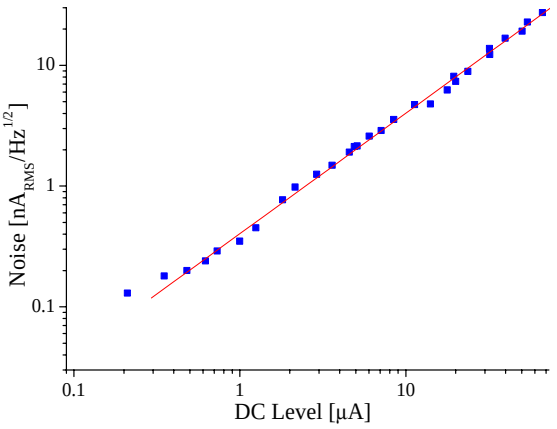

Figure 2. Noise vs. DC level.

For the purposes of definition, Figure 3 shows schematically the elements of the CPT resonance signal. The CPT spectrum is dominated by the Gaussian laser absorption feature, whose width may be several GHz due to a combination of Doppler and pressure gas broadening. The Lorentzian CPT signal sits atop the Doppler absorption feature and is characterized by its amplitude, designated "Signal," and linewidth, γ. We define the "contrast," η, of the CPT resonance as Signal divided by DC level.

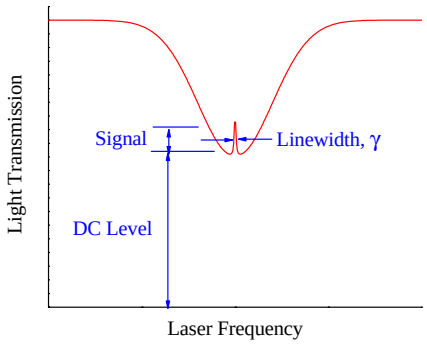

Figure 3. CPT resonance features.

With these definitions, and the aforementioned linear relationship between DC level and noise, we arrive at the appropriate figure-of-merit, ξ, for predicting short-term stability of the CSAC:

$$\xi = \eta / \gamma ,$$

where η and γ are measured in ppm and Hz respectively. This leads to the relationship

$$\sigma_y(\tau) \propto \frac{1}{\xi} \tau^{-1/2} ,$$

where the constant of proportionality is determined by the spectrum of frequency noise on the VCSEL. This presents a valuable relationship, from the perspective of CSAC engineering, in that it permits the evaluation of different atomic transitions and species and operating conditions without explicit dependence on the noise properties of the particular laser source employed in the measurement.

LABORATORY TESTBED

We have improved our laboratory CSAC testbed over the past year, in order to better support precision CPT resonance spectroscopy and evaluation of prototype components. Figure 4 below shows a layout of the experimental setup as configured for spectroscopic measurements.

The experimental testbed includes independent temperature-stabilized assemblies for the VCSEL and resonance cell as well as a separate reference cell, containing cesium and buffer gas, which allows consistent and reproducible laser stabilization independent of the laser intensity, vapor density, and geometric characteristics of the resonance cell. A variable attenuator at the input to the reference cell allows for two orders of magnitude of intensity variation. The RF chain provides microhertz resolution tunability at 4.6 GHz, with negligible offset and phase noise, continuous power adjustment to +20 dBm, and modulation and sweep capabilities. The VCSEL is locked to the reference cell by applying audio frequency modulation to its drive current, synchronously detecting the response from the reference cell and applying a correction to the bias current from the proportional/integral loop filter.

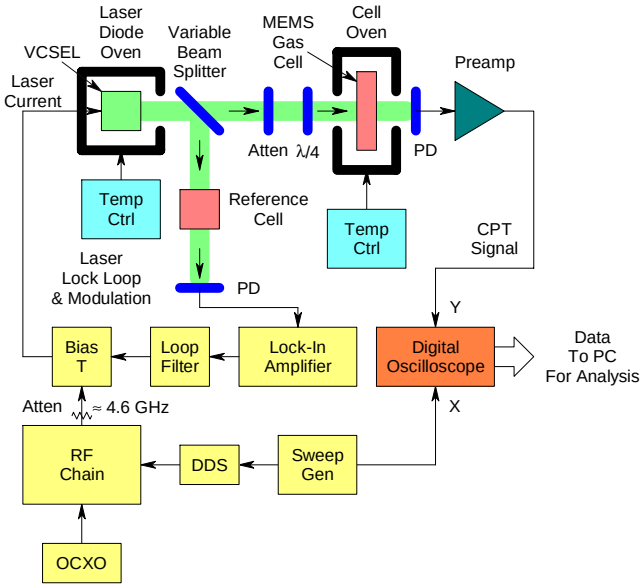

Figure 4. Testbed configured for CPT spectroscopy.

The RF frequency is repetitively swept across the CPT resonance while the cell transmission is collected and averaged on a digital storage oscilloscope. The data are transferred to a personal computer for subsequent analysis and archive.

Figure 5 shows a typical CPT signal, measured on the D1 resonance of cesium at λ = 894 nm in a small glass cell with 1 mm path length, similar to that shown in Figure 5 of reference **[1]**, containing cesium and 50 torr of buffer gas at a temperature of 75°C. Also shown in the figure is a fit to a Lorentzian lineshape. The fit demonstrates a linewidth of γ = 879 Hz and peak contrast η = 7828 ppm, with reduced-χ^2 = 0.996. Note that this measurement leads to a figure-of-merit of ξ = 8.9.

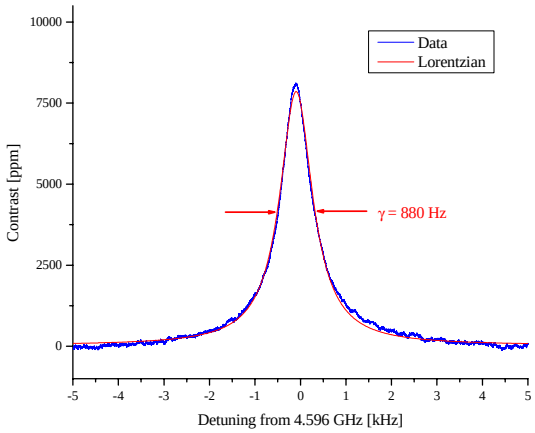

Figure 5. CPT resonance signal.

D1 VS. D2 EXCITATION

There are two principal optical transitions, accessible with diode laser technology, which could be employed for CPT interrogation of the cesium ground-state hyperfine resonance. These two, termed "D2" and "D1," are shown in Figure 6. Research on a similar alkali system, rubidium, has indicated that the D1 CPT transition exhibits a narrower linewidth and higher contrast than D2, both of which contribute to higher ξ **[2]**. Because the cesium structure is substantially similar to that of rubidium, a similar improvement could be expected in cesium CPT spectroscopy, though to some lesser extent, due to the higher degeneracy and details of the cesium hyperfine structure. Prior to this work, all published data of CPT spectroscopy in cesium were performed on the D2 line, due to the availability of 852 nm laser devices. In the past year, we have developed VCSEL devices at 894 nm, permitting a direct comparison of the performance advantages to a CSAC based on either transition.

Figure 6 shows the transitions of the cesium atomic structure relevant for CPT interrogation, including both the "D1" and "D2" principal optical transitions at λ = 894 nm and λ = 852 nm, respectively, each of which contains a cluster of hyperfine states.

The D2 optically excited 6 $P_{3/2}$ state is composed of four angular momentum substates, F=2-5, while the D1 optically excited 6 $P_{1/2}$ state is composed of only two sub-states, F=3, 4. The optical dipole selection rules, applicable to CPT interrogation, limit the participating excited state transitions to F =3,4. The additional F=2 and F=5 excited state components in the D2 manifold scatter light, reducing the available atomic population without contributing to the CPT signal, thus reducing the contrast. In addition, the F=2 and F=5 excited states in D2 provide a pathway for CPT decoherence, resulting in a broader resonance line.

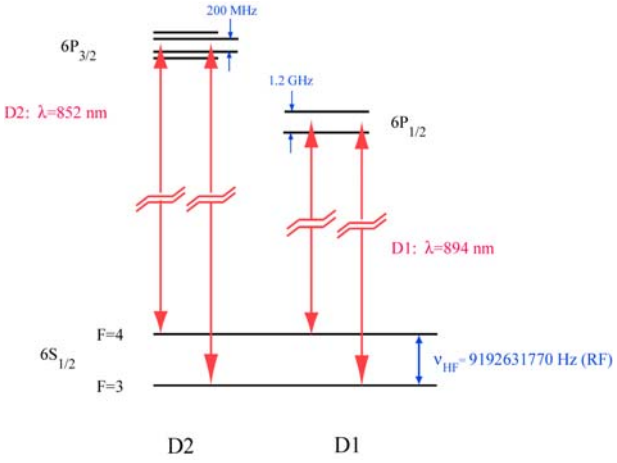

Figure 6. Cesium D1 and D2 CPT resonance levels.

Note that the spacing of the F=3 and F=4 excited-state transitions is 6X wider in the 6 $P_{1/2}$ (D1) manifold than in 6 $P_{3/2}$ (D2). In a Doppler-broadened gas cell, the inhomogeneous atomic linewidth is roughly 400 MHz and the D1 lines, which are separated by 1.2 GHz, are fully resolved while the D2 lines, separated by only 200 MHz, are not. As a result, in a Doppler-broadened cell, the D2 CPT resonance operates simultaneously on both excited-state transitions, while the D1 does not, thus reducing the effective transition strength of D1 excitation by a factor of 2. This detrimental effect is somewhat reduced in the CSAC, wherein the additional inhomogeneous line broadening due to the necessarily high buffer gas pressure limits the resolution of the D1 transitions.

The relative advantage of D1 CPT interrogation is less pronounced in cesium than in rubidium for several reasons. First, note that the Zeeman degeneracy of both the ground and excited states limits the fraction of optical signal that contributes constructively to the CPT resonance signal. Because the cesium system has higher degeneracy than rubidium, not only is the signal contrast lower for both D1 and D2 excitation, but the relative advantage of D1 is also proportionately reduced. Secondly, in rubidium the splitting of the $P_{1/2}$ sub-levels is only 800 MHz and the Doppler width is 500 MHz, so that both components contribute to the D1 CPT resonance signal, even at relatively low buffer gas pressure.

The D1 VCSELs, developed at Sandia National Laboratories in support of this program, have been optimized in several respects to support the CSAC architecture. The 1-λ cavity length ensures that the VCSELs operate in a single longitudinal mode and, thus, are free of the "mode-hopping" behavior that characterizes conventional cleaved facet edge-emitting laser devices. The CSAC requirements impose additional demands on the optical performance of the laser device, including that it must operate on a single transverse cavity mode, that the polarization remain stable, and that the wavelength tune to the cesium atomic resonance over life and at the operating temperature of the physics package. In addition to these optical requirements, the devices have been optimized for high efficiency to meet the stringent power requirements of the CSAC application, delivering 100 μW of optical power while dissipating only 2 mW, and for high modulation efficiency, producing optimal sideband amplitude with less than 1 mW of RF drive power at 4.6 GHz. Figure 7 below shows a representative photograph and light-current-voltage data for the devices developed for the CSAC program.

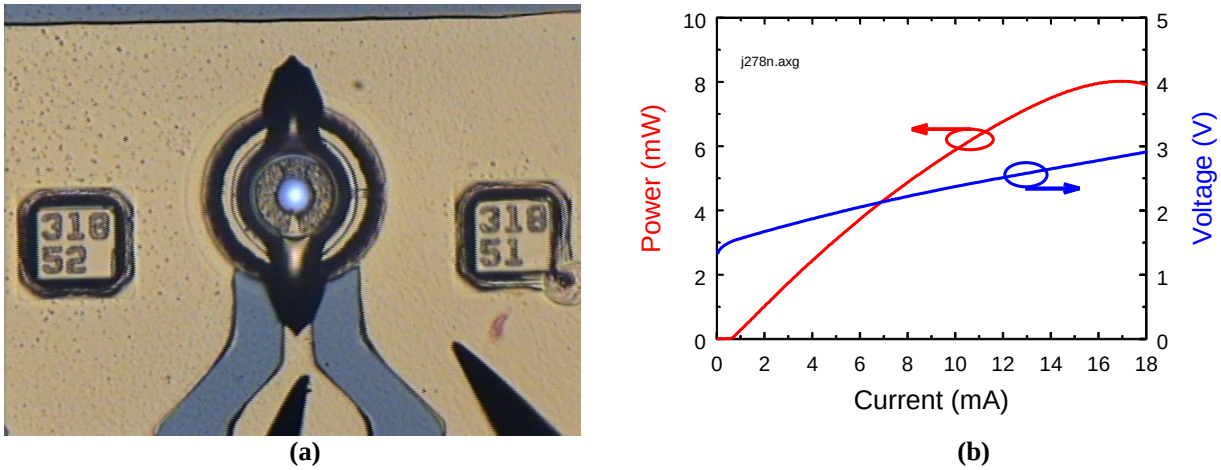

Figure 7. Prototype VCSEL device (a) photograph and (b) light-current-voltage data.

The D1 VCSELs were fabricated using the same semiconductor processing steps as for 850-nm oxide-aperture VCSELs. The oxide aperture simultaneously confines both the current and the optical mode, thereby resulting in lower threshold currents than VCSELs that use proton implantation to create a current aperture. In order to reach a wavelength of 894 nm, the epitaxial semiconductor structure was modified slightly from the standard 850-nm design. The VCSEL was grown on a semi-insulating GaAs substrate to minimize the parasitic capacitance of the wire-bond pads. The bottom distributed Bragg reflector (DBR) is designed as a high reflector, containing 36 pairs of n-doped quarter-wave $Al_{0.16}Ga_{0.84}As$ and $Al_{0.92}Ga_{0.08}As$ layers. The active region contains 5 $In_{0.07}Ga_{0.93}As$ quantum wells, each 6-nm thick, producing a room-temperature optical gain peak near 885 nm. A quarter-wave layer of $Al_{0.98}Ga_{0.02}As$ immediately above the active region is selectively oxidized to form a circular oxide aperture. The oxide aperture diameter is kept below 4 microns to force the VCSEL to operate only in the fundamental transverse mode. The top DBR is designed as an output coupling mirror, containing 21 pairs of p-doped quarter-wave $Al_{0.16}Ga_{0.84}As$ and $Al_{0.92}Ga_{0.08}As$ layers (in the pair immediately above the active region, the $Al_{0.92}Ga_{0.08}As$ layer is replaced with $Al_{0.98}Ga_{0.02}As$). The doping levels in the DBRs are lower than in typical commercial devices in order to obtain higher conversion efficiency.

For the measurements reported below, the Sandia D1 VCSEL is compared with a D2 VCSEL manufactured by the MODE corporation **[3]**. The two devices are similar, though the Sandia device is

roughly 10X more efficient, both at DC and RF, and exhibits a 5X higher noise floor, due perhaps to increased sensitivity to noise on the DC bias current associated with the higher device bandwidth. The noise performance, which is an area of ongoing improvement, has no impact on the measurements contained herein due to our definition of the figure-of-merit, ξ, which is independent of the actual noise figure of the laser source.

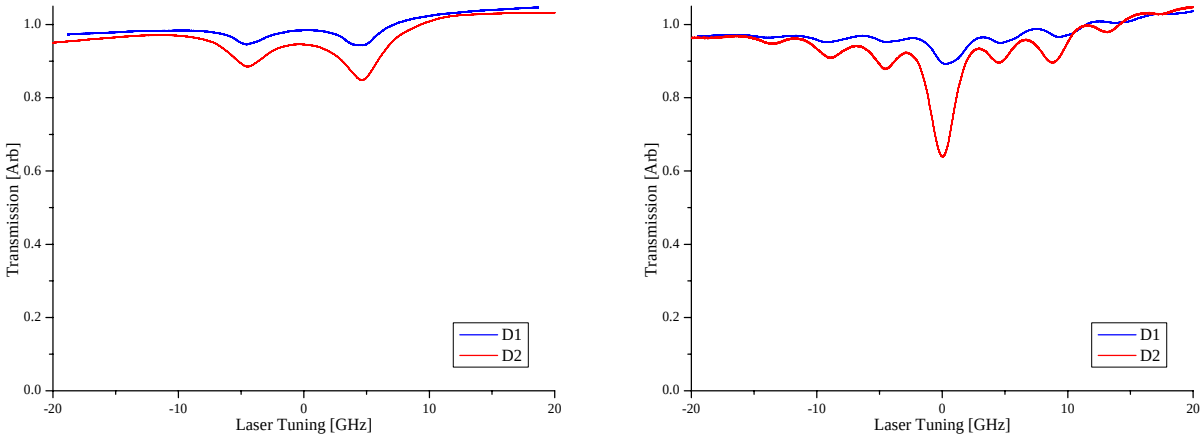

Figure 8. D1 vs. D2 optical absorption spectra with (a) RF off and (b) RF on.

Figure 8(a) and (b) show the laser absorption spectra as the laser frequency is swept across the D1 and D2 transitions with the 4.6 GHz RF drive off and on, respectively. In all cases, the resonance cell was the small glass cell from reference **[1]**, filled with cesium and 70 torr of a temperature-compensated nitrogen/argon buffer gas mixture at our design operating temperature of 65°C. Note that the D2 absorption is roughly 4X that of D1, due partly to the aforementioned resolution of the D1 excited states and partly due to additional scattering from the F=2 and F=5 substates of D2.

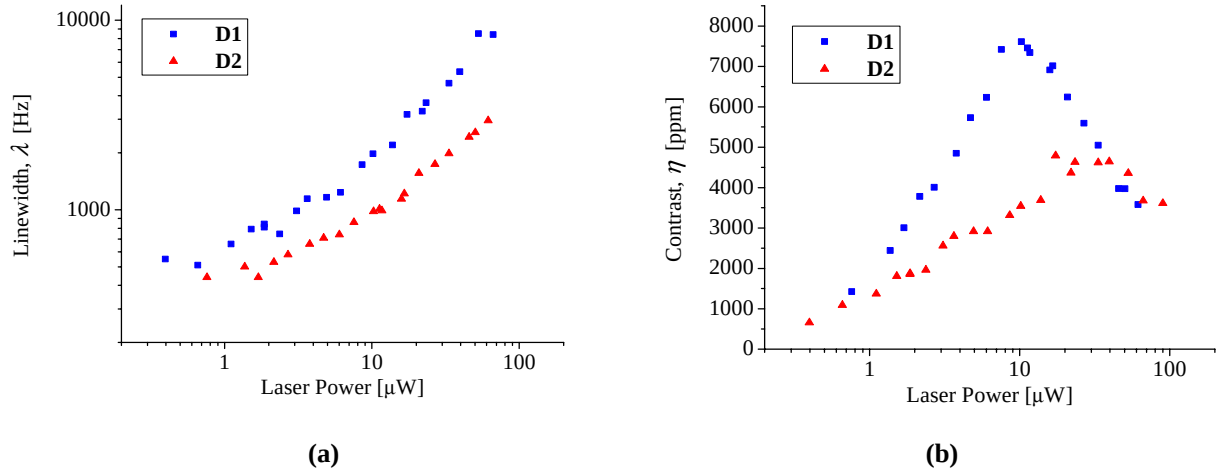

Figure 9. D1 vs. D2 CPT resonance (a) linewidth and (b) contrast vs. laser power.

Figures 9(a) and (b) show the measured linewidth and contrast for the D1 and D2 transitions. Note that in both cases the linewidth appears to exhibit a simple power-law relationship to the laser power, due to optical power broadening of the optical resonance. At low laser power, the linewidth is limited to $\gamma \approx 500$ Hz due to cesium-cesium (spin exchange) collisions in the vapor cell. If necessary, the linewidth can be further reduced by lowering the cell temperature, at the expense of both signal and contrast, and thus ξ. In both the D1 and D2 cases, the contrast improves with increasing laser power until the point at which the atomic sample is fully utilized, at which point the DC level continues to increase without increase in signal. The results of Figure 9 are combined to produce our figure-of-merit, shown below in Figure 10.

Our results indicate a 3-4X advantage for CSAC of employing the D1 transition instead of the D2 transition. In both cases, the optimum laser power is less than 10 μW, though the slightly higher optimum power level of D1 is an additional advantage in that it provides a higher signal level into the signal recovery electronics.

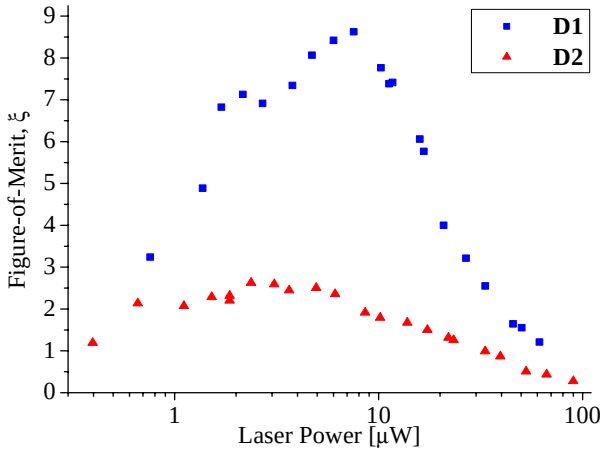

Figure 10. D1 vs. D2 figure-of-merit vs. laser power.

MEMS CELL FABRICATION

In addition to the power and stability requirements, it is also important that the CSAC design be cost-effective for high-yield large-volume production. Towards this goal we have begun development at Draper Laboratory of a silicon-glass cesium resonance cell, utilizing the manufacturing techniques of micro-electromechanical systems (MEMS). The proposed manufacturing scheme is illustrated below.

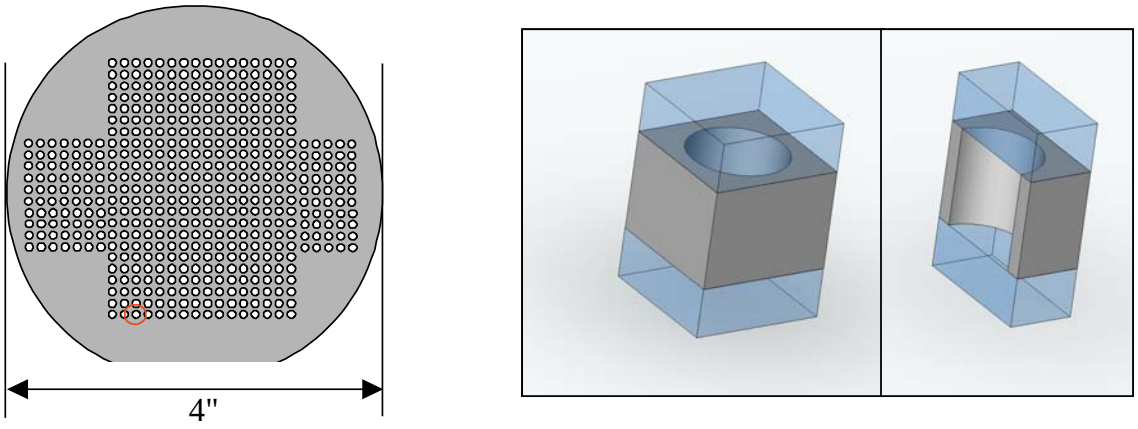

Figure 11. MEMS cell fabrication concept.

Figure 11 illustrates the planned methodology for large-scale production of cesium resonance cells for CSAC. On the left, (a), an array of approximately 500 1.5 mm holes is etched into a 1.5 mm thick 4" diameter silicon wafer by the technique of deep reactive ion etching (DRIE). A 4"Pyrex wafer is bonded to the bottom of the wafer using the vacuum tight technique of anodic bonding. The cesium and buffer gas are introduced into the cells and then a second Pyrex wafer is bonded to provide the upper window and complete the vacuum seal. The cells are then diced from the wafer for subsequent incorporation into the CSAC. Figure 11(b) shows isometric and cross-sectional views of a single diced cell.

While these techniques for batch fabrication are under development, we have begun experimentation in the CSAC testbed system with prototype cells of isomorphic geometry and material composition. Prototype cells were manufactured via a hybrid process of MEMS cell fabrication combined with conventional glassblowing and cell processing techniques.

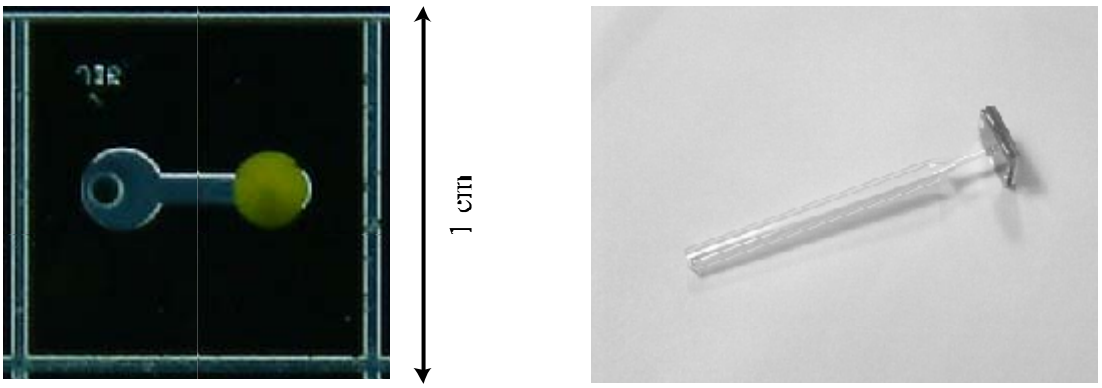

Figure 12. MEMS prototype cell components – (a) micromachined silicon wafer and (b) tubulated cell.

Photolithography followed by DRIE was employed to create the dumbbell pattern in the silicon substrate, as shown in Figure 12 (a). On the right-hand side, a 1.5 mm diameter hole is etched all the way through the 1.5 mm thick silicon wafer. This is connected, via a 1 mm wide by 100 μm deep pathway, to a second 1.5 mm aperture, also only 100 μm deep. The top and bottom Pyrex wafers are attached via anodic bonding as described above, only the top plate has been ultrasonically drilled with an array of 0.5 mm holes that align with the shallow "fill" area of the dumbbells. After the anodic bonding process is complete, the cells are diced from the wafer into 1 cm squares, each containing a single 1.5 mm diameter × 1.5 mm thick resonance cell, with a small additional volume accommodating the tubulation and attachment. Tubulations are individually attached to each cell using conventional glassblowing techniques, as shown in Figure 12(b), and the cells are filled with cesium and buffer gas using a conventional glass manifold processing system. The resultant cell is shown below in Figure 13.

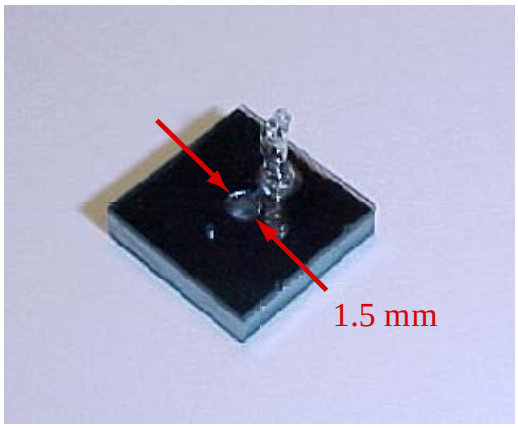

Figure 13. Prototype silicon-glass MEMS cell.

Figure 14 reflects efforts in our laboratory to measure narrow linewidths in the MEMS cell. The cell employed for this measurement has an elliptical cross section, 2 mm × 3 mm, and 800 μm path length. The cell contains cesium and 90 torr of temperature-compensated N_2/Ar buffer gas mixture. The cell is stabilized at our designed operating temperature of 65°C and illuminated with only 1.2 μW of laser power. The fit to a Lorentzian lineshape has a reduced-χ^2 = 0.98 and indicates a linewidth of γ = 438 Hz and peak contrast η = 110, leading to ξ = 0.25.

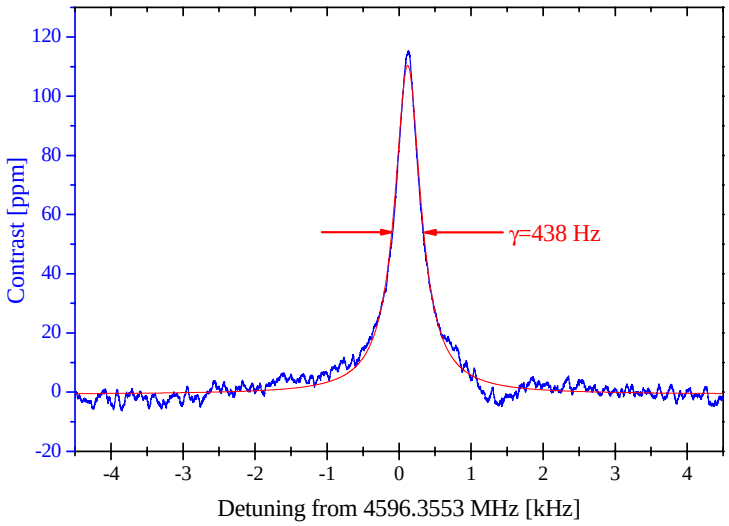

Figure 14. Relatively narrow CPT resonance in MEMS cell.

As discussed earlier, it is possible to observe even narrower linewidths at the expense of ξ, and thus clock stability. By reducing the cell temperature to 50°C and the laser power to 500 nW, we have observed linewidths as narrow as 265 Hz in similar micromachined silicon-glass cells, though at values of $\xi < 0.03$ with little practical value for CSAC application.

Our laboratory CSAC testbed can be configured to operate as a closed-loop frequency standard, as shown in Figure 15. Our experimental setup for stability measurements is similar to that used for spectroscopy (compare Figure 4) with the following alterations. Rather than sweeping the 4.6 GHz RF frequency and observing the cell transmission on an oscilloscope, the RF is sinusoidally modulated at a rate 500 Hz and depth of 1 kHz. The detected signal is coherently demodulated by a lock-in amplifier and the resultant error signal is integrated by the loop filter and fed back to the 5 MHz quartz oscillator, which serves both as the reference signal to the RF system and provides a buffered output for direct comparison with our house standard hydrogen maser via standard frequency measurement techniques.

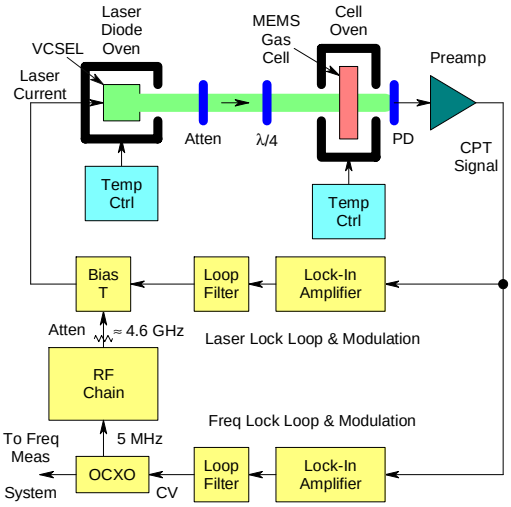

Figure 15. Testbed configuration for closed-loop operation.

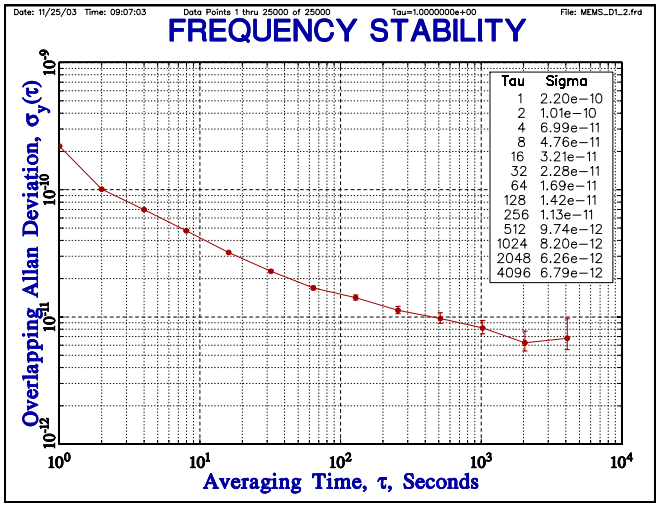

Figure 16. Frequency stability of CSAC testbed with MEMS cell.

Figure 16 shows the Allan deviation for the CSAC testbed, utilizing the MEMS prototype cell, D1 laser excitation, and typical operating parameters for temperature and laser intensity. For this 12-hour measurement, the cell employed had a 1.5 mm diameter aperture, a 1.5 mm path length, and was stabilized at T = 70°C. The laser power was 20 μW and the figure-of-merit of the resonance signal was $\xi = 3.2$. At short times, the frequency stability displays the $\tau^{-1/2}$ behavior that typifies atomic frequency standards and displays a 1-second intercept of $\sigma_y(\tau=1) = 1.5\times10^{-10}$, roughly 4X margin over our design goal of $\sigma_y(\tau=1) = 6\times10^{-10}$. We expect that further optimization of cell geometry, buffer gas pressure, and laser intensity will lead to further improvement in ξ and, thus, σ. At longer times (>1000 seconds), the device exhibits flicker behavior, reflecting environmental sensitivity, most likely due to

thermal variation in the required bias voltage of the VCSEL. We expect this medium-term environmental sensitivity to be greatly reduced when the thermal isolation of the physics package is implemented in the next phase of the CSAC development effort.

CONCLUSIONS

We have performed an experimental comparison of the D1 and D2 cesium CPT resonances in a CSAC experimental system and have found the D1 resonance to provide a 3-4X better figure-of-merit for CSAC stability. We have developed prototype silicon-glass MEMS cells and verified short-term stability utilizing these cells as well as the low-power VCSEL devices designed for implementation in the CSAC. At this point, we have tested all of the key physics package components necessary to implement a small low-power CSAC and have found them capable of supporting the performance and power goals of the project.

ACKNOWLEDGMENTS

The authors wish to thank Mike Garvey, of the Symmetricom TRC, and Jim Sitomer of Draper Laboratory, for supporting and directing this effort. We are also grateful for the exceptional glass-blowing skills of Patrick DeFlorio of the Yankee Glassblowing Company and of Luke Tomlin and Joe Reid of the Symmetricom TRC. E. L. Blansett of Sandia National Laboratories contributed to investigations of polarization stability in our VCSEL development. This work is supported by the Defense Advanced Research Projects Agency, Contract # NBCHC020050.

REFERENCES

[1] R. Lutwak, et al., 2003, *"The Chip-Scale Atomic Clock – Coherent Population Trapping vs. Conventional Interrogation,"* in Proceedings of the 34th Annual Precise Time and Time Interval (PTTI) Systems and Applications Meeting, 3-5 December 2002, Reston, VA, USA (U.S. Naval Observatory, Washington, D.C.), pp. 539-550.

[2] M. Stahler, et al., 2002, *"Coherent population trapping resonances in thermal ^{85}Rb vapor: D_1 vs D_2 line excitation,"* **Optics Letters, 27,** 1472-1474.

[3] MODE Corporation, Product Number 8085-1000.